A Mechanistic Model for Predicting Flow-assisted and General Corrosion of Carbon Steel in Reactor Primary Coolants

D. H. Lister and L.C. Lang***

Introduction

In CANDU reactors, the piping that connects the in-reactor fuel channels to the steam generators is made of grade SA106-B carbon steel with a maximum level of impurity cobalt specified to minimise activity transport. In the CANDU-6 design, there are 380 fuel channels containing the Zr-2½Nb pressure tubes; they are arranged horizontally in the cylindrical calandria vessel that holds the D_2O moderator at about 65°C. Each pressure tube holds twelve Zircaloy-4 fuel bundles, fuelled with natural-U UO_2, which are placed end to end and replaced on-power by means of fuelling machines that lock onto the ends of the fuel channel.

Either face of the reactor has 190 outlet feeders and 190 inlet feeders directing the D_2O coolant to and from two steam generators, via headers, at 310°C and 265°C respectively. The inlet feeders are mostly 5.7 cm internal diameter (I.D.); the outlets are mostly 6.4 cm, with several 5.0 cm, and generally have an expansion to 7.6 cm or 8.9 cm at several m from the core. Connections to the pressure tube end fittings are made with Grayloc connectors. The coolant is kept at a constant pHa (apparent pH of D_2O – measured at room temperature with an electrode calibrated in H_2O solution); the value is between 10.3 and 10.8 achieved with additions of lithium, and hydrogen gas is added to between 3 and 10 mL/kg. Bulk boiling occurs in the fuel channels producing up to 6 wt% steam quality in the outlet feeders; this persists up to the steam generators, where it collapses in the hot leg of the U-tubes.

The four steam generators in the overall primary circuit are tubed with Alloy-800 that also has a specification for low cobalt. There are two coolant loops, each with a steam generator at either face of the reactor, but they are interconnected with piping that incorporates the pressurizer and purification circuit. Figure 1 illustrates the piping arrangement at a reactor face.

Since the start-up of the first CANDU-6s in the early 1980s, all of their systems have undergone regular inspections. For the feeders, this has entailed ultrasonic measurement of wall thickness at selected accessible bends close to the headers but distant from the core (see Figure 1). No untoward corrosion was ever found there. At Point Lepreau in 1996, however, when measurements were made adjacent to the pressure–tube end fittings at the reactor face, substantial wall thinning of the outlet feeders was recorded.

No attack on the inlet feeders was evident. The thinning rates, deduced from the measurements, from estimates of initial thickness and from operating time, varied between about 40 and 140 □m/a. Since the rate was strongly correlated with coolant velocity (to the power 1.52 - see Figure 2), the phenomenon was deemed flow-assisted corrosion (FAC). Inspections at other CANDUs have since confirmed that the phenomenon is widespread.

At such thinning rates, the long-term integrity of the feeder system is threatened. In particular, the extrados regions of the outlet bends, which started out thin because of the pipe-forming operations, could reach their minimum allowable wall thickness within the operating lifetime of the plant, necessitating expensive shut-downs for replacement. Programs to investigate the causes and develop mitigation strategies are now in place within the industry in Canada. The model described in this paper is a development of the associated research program at the University of New Brunswick.

* Department of Chemical Engineering, University of New Brunswick, Fredericton, N.B., Canada, E3B 5A3
** Atomic Energy of Canada, Ltd., Chalk River Laboratory, Chalk River, Ont. Canada, K0J 1J0

Carbon Steel Corrosion – General Principles

Under alkaline, reducing conditions in high-temperature water, carbon steel develops a corrosion film of magnetite. As observed in experiments in closed and static systems, such as loops and autoclaves, and as found in boiler systems, the film is typically double-layered with the Potter-Mann structure (Potter and Mann, 1963). The inner-layer magnetite, adjacent to the metal, is fine-grained and grows at the metal-oxide (M-O) interface. The outer layer magnetite is precipitated from solution at the oxide-coolant (O-C) interface and is composed of crystallites, generally octahedral in shape, of a few □m in size.

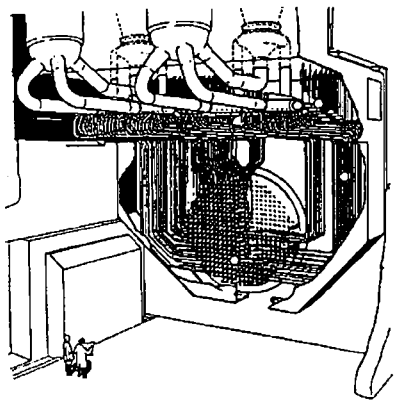

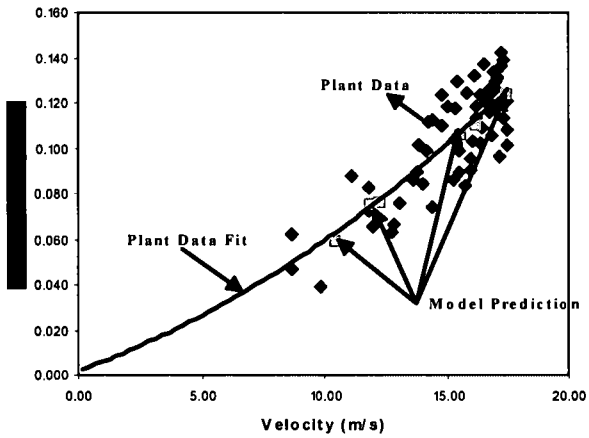

Figure 1. Candu-6 Reactor Face, Feeder Arrangement.

Figure 2. Outlet Feeder Thinning Rate and Coolant Velocity at Point Lepreau.

The magnetite is formed via the overall reaction scheme:

$$3Fe + 4H_2O = Fe_3O_4 + 4H_2 \quad (1)$$

Most (about 88%) of the hydrogen is probably generated at the M-O interface as iron goes into solution:

$$Fe + 2H_2O = Fe^{2+} + 2OH^- + H_2 \quad (2)$$

and as about one half of the ferrous species precipitates there, taking up the volume of the metal corroded:

$$3Fe^{2+} + 6OH^- = Fe_3O_4 + 2H_2O + H_2 \quad (3)$$

In fact, Tomlinson (1981) has observed that up to 90% of corrosion hydrogen is dissipated through the steel, adding weight to the argument for its generation at the M-O interface, since it must be incorporated in the metal in the atomic state, i.e., immediately on formation. An alternative oxidant to H_2O at the M-O interface has been proposed; protons (H^+) may diffuse inwards across the film and be discharged as hydrogen atoms (Tomlinson, 1981). A totally different mechanism, relying on the inward diffusion of oxide ions, O^{2-}, along grain boundaries

(Effertz, 1972), suffers from the disadvantage that O^{2-} transport is too slow to account for observed corrosion rates (Robertson, 1989) and in any case cannot account for hydrogen generation at the M-O interface. The fate of the generated hydrogen, the dissipating portion of which depends on the availability of a sink at the outside of the metal, is important for the formation of the corrosion film and the details of the corrosion mechanism (Bloom, 1960; Berge et al, 1976).

The ferrous species not precipitated at the M-O interface diffuse through the film to precipitate at the O-C interface, generating the last 12% of the hydrogen. This iron diffusion is generally believed to control the corrosion (Castle and Mann, 1966; Castle and Masterson, 1966; Bignold et al., 1978; Tomlinson, 1981; Robertson, 1989).

Robertson (1989) has suggested that the main pathway for iron migration across the film is via magnetite grain boundaries, involving Fe^{2+} diffusion by a solid-state vacancy mechanism. Charge balance then requires a compensating inward flux of positive ions (presumably protons, H^+) or an equivalent outward flux of negative ions (presumably electrons or hydroxyl ions, OH^-). The rationale for this "grain-boundaries" model is the similarity of activation energies for steel corrosion in steam and water – the former necessarily occurring by solid-state processes. Also, the pores of the inner magnetite layer are apparently rather small to allow dissolved iron species to diffuse freely in solution (less than 1 nm in diameter – at least, in near-neutral solutions (Tomlinson, 1981)).

The alternative route in steel corrosion in water for iron migration across the film involves the diffusion of dissolved ferrous species in the liquid phase through pores in the magnetite. This "pores-solution" model will be tenable if the diffusion processes realistically account for the observed corrosion rates. In fact, the electrochemistry within the magnetite film adequately influences the diffusion driving forces – as we demonstrate later. Also, for situations of interest here, the pores should be large enough to accommodate the diffusion. Recent measurements (Mayer, 2001) indicate that inner-layer magnetite formed under FAC conditions has crystallites as small as 10 nm. The interstices, however, should be generally larger than 1 nm while irregularities of crystallite growth and stacking should allow adequate porosity to reach the M-O interface.

Flow-Assisted Corrosion in CANDU Feeders

The feeder thinning phenomenon has much in common with FAC in secondary coolants. The magnetite films that develop on surfaces are thin and single-layered, in contrast with those formed during general corrosion. Also, besides the strong dependence on coolant flow rate (to the power of ~1.5 of the velocity, as mentioned earlier), attacked surfaces are characteristically scalloped. The scallops on the 6.4 cm outlet feeder S08 removed from the CANDU-6 reactor at Point Lepreau in 1997 are about 0.6 mm across and 0.2 mm deep (Burrill and Cheluget, 1998). That particular feeder, which holds coolant flowing at an average velocity of 16.2 m/s (up to the expansion) and with an average steam quality up to 4 wt%, is estimated to have undergone FAC at the extrados of the first bend (about 15 cm downstream of the Grayloc) at an average rate of 110 □m/a since the startup of the reactor in 1982. However, across all the feeders in the reactor, no obvious correlation of FAC rate with steam quality has emerged, while the evidence from several CANDUs indicates that the effect of pH within the operating range is weak – if it exists at all (there is the possibility that somewhat lower average FAC rates at one CANDU-6 can be attributed to a generally lower pH within the range over the operating life of the reactor (Elliott, 2000)).

A pH effect is to be expected from the change in solubility of magnetite over the temperature range across the core, since at CANDU conditions solubility rises with temperature (Sweeton and Baes, 1970; Tremaine and Leblanc, 1980). For example, at an operating pH_a of 10.7, the coolant entering the core at 265°C should be saturated in dissolved iron at about 13 ppb (according to Sweeton and Baes, 1970). At the reactor outlet, the temperature has risen to 310°C and the solubility is about 24 ppb. Since there is hardly any source of iron in the core (because the fuel channel is made mostly of zirconium alloys) the outlet coolant is undersaturated to the extent of 11 ppb and there is a driving force for FAC to occur. It should be noted that, unlike secondary-side FAC at lower temperatures, feeder thinning should be exacerbated by higher pH.

Material effects seem to be important in feeder FAC, too. The specification of low-cobalt steel has meant that chromium levels also are low (< 0.03 wt%), which has exacerbated the corrosion. The effect is illustrated by the contrasting FAC rates of the removed feeder SO8 and the Grayloc connector to which it was welded. The latter contained about 0.13 w% Cr and suffered much less attack (Lister et al., 1998).

Not surprisingly, attempts at modelling feeder thinning have so far been based on the typical steady-state approach to describing secondary-side FAC. Thus, before FAC of outlet feeders was discovered, general feeder corrosion had been modelled as two transport resistances in series – film dissolution followed by mass

transfer from the O-S interface to the bulk coolant (Burrill and Turner, 1994). Following the ideas of Berge et al. (1980), the metal oxidation rate was assumed to be twice the film formation rate at the M-O interface which, at steady state, equals the dissolution rate. By using system parameters and oxide properties appropriate to the CANDU primary coolant, including a dissolution rate constant for magnetite determined experimentally at high temperature by Balakrishnan (1977), Burrill and Turner (1994) predicted feeder corrosion rates that were quite low – even though the resulting fouling of the system with corrosion products was high, as was, in fact, observed.

A parallel approach in our laboratory (Lister et al., 1994) resulted in a somewhat modified equation for steady-state corrosion rate, $\frac{dm}{dt_{ss}}$, in terms of film dissolution and mass transfer:

$$\frac{dm}{dt_{ss}} = \frac{C_{eq} - C_b}{\frac{0.43}{k_d F^*} + \frac{1}{k}} \qquad (4)$$

where C_{eq} = magnetite solubility;
C_b = bulk coolant concentration of dissolved iron;
k_d = magnetite dissolution rate constant;
F^* = surface area factor for O-C interface (= $\sqrt{3}$ for a regular array of octahedra);
k = mass transfer coefficient.

The difficulty with these approaches becomes clear when Equation 4 is evaluated; a corrosion rate of 2 □m/a is obtained, film dissolution controls, since k_d . 1.3 x 10^{-2} mm/s while k . 10 mm/s, and there is no discernable influence of fluid flow. Even after the addition of an empirical erosion term to Equation 4, obtained by scaling, according to fluid shear stress, the results of corrosion tests at high coolant velocity in an isothermal, iron-saturated loop (Kenchington et al., 1983), the maximum corrosion rate predicted (i.e., for a 17 m/s feeder) is only 30 □m/a though there is a parabolic dependence of corrosion rate on flow. While these predictions at the time instilled some confidence that feeders were behaving within their allotted bounds, the discovery of FAC in 1996 showed that they were inadequate. New thinking was required.

Limitations with models of the type exemplified by Equation 4 to some extent involve the validity of the data. The mass transfer coefficient, k , although calculated from well-established correlations, will not have been independently verified at the extreme condition of CANDU coolant. Furthermore, even if mass transfer controlled, the velocity dependence would be too low (correlations such as that of Berger and Hau (1977) indicate a dependence of k on the power 0.86 of the velocity). On the other hand, the additive erosion term described above gives a velocity dependence that is too high (parabolic) and, in any case, was obtained from experiments under non-FAC conditions. Lister et al. (1997) obtained an intermediate velocity dependence – as observed – by assuming that magnetite dissolution proceeds and weakens the film sufficiently to allow spalling to occur. The film builds up to a limit and then spalls to a minimum thickness. The limit is determined by the time between spalling events and governs the average film thickness, which determines the corrosion rate. That spalling time is assumed to be proportional to the fluid shear stress, as determined by the friction factor, and the proportionality constant was obtained by fitting the model to the observations of the feeder S08 removed from the Point Lepreau reactor. An excellent fit to the data shown in Figure 2 was obtained. It must be remembered, however, that the magnetite dissolution parameters k_d and C_{eq} have been obtained from experiments on "bulk" (i.e., powdered or granulated) material; because the dissolution is a reductive process (the reverse of Equation 3) the parameters applicable to a corrosion film must depend on the electrochemical corrosion potential (ECP) of the surface, in other words, on the corrosion rate itself, since corrosion determines ECP. Burrill and Cheluget (1998) addressed this issue by inserting a potential-dependent multiplier of the solubility into their version of Equation 4, which indicated a strong dependence of solubility on corrosion rate. We account for such electrochemical considerations in the following comprehensive model that develops the concept of the 1997 (Lister et al.) paper.

The Mechanistic Model

Transport Equations for General Corrosion (Inlet Feeders)

Since the inner oxide layer replaces the volume of metal corroded, for a corrosion rate $\frac{dm}{dt}$ the rate of growth at the M-O interface is given by:

$$\text{Input of iron to inner layer} = 0.723\frac{\rho_{ox}}{\rho_{Fe}}(1-\Phi_i)\frac{dm}{dt} \tag{5}$$

Where:
- 0.723 = mass fraction of iron in magnetite;
- ρ_{ox} = density of magnetite (= 5.2 g/cm^3);
- ρ_{Fe} = density of metal (= 7.9 g/cm^3);
- Φ_i = porosity of inner layer

$$\text{Therefore, growth at M-O interface} = 0.476(1-\Phi_i)\frac{dm}{dt} \tag{6}$$

and the remaining corroded iron diffuses outwards through the pores:

$$\text{diffusion rate} = \frac{dm}{dt} - 0.476(1-\Phi_i)\frac{dm}{dt}$$

$$= 0.476(1.101+\Phi_i)\frac{dm}{dt} \tag{7}$$

An outer oxide layer precipitates on top of the inner layer under iron-saturated conditions (as found in the inlet feeders). Including the diffusional resistances of the inner and outer layers of thickness □$_i$□and □$_o$, respectively, along with mass transfer to the bulk coolant where the dissolved iron concentration is C_b, the expression for corrosion rate from Equation 7 becomes:

$$\frac{dm}{dt} = \frac{S.C^e_{m-o} - \dfrac{(k_pF^*C^e_{o-c} + kC_b)}{(k_pF^* + k)}}{0.476(1.101+\Phi_i)\left[\dfrac{\delta_i\zeta}{\rho_{ox}(1-\Phi_i)\Phi_iD_{Fe}} + \dfrac{\delta_o\zeta}{\rho_{ox}(1-\Phi_o)\Phi_oD_{Fe}} + \dfrac{1}{(k_pF^* + k)}\right]} \tag{8}$$

where:
- S = supersaturation factor to account for small crystallite size (assumed 1.1);
- C^e_{m-o} = solubility at M-O interface;
- C^e_{o-c} = solubility at O-C interface;
- k_p = precipitation rate constant; initially assumed same as Balakrishnan's (1970) dissolution rate constant, corrected to reactor inlet temperature with an Arrhenius extrapolation;
- k = mass transfer coefficient (calculated from a correlation such as that of Berger and Hau (1977) or, to take into account mass transfer enhancements due to surface roughness effects, the correlation of Poulson (1990));
- F^* = surface area factor (assumed $\sqrt{3}$, as for a regular array of octahedra);
- ζ = tortuosity (assumed 1.2 for both layers);
- Φ_i = porosity of inner layer (assumed 0.1);
- Φ_o = porosity of outer layer (assumed 0.3);
- D_{Fe} = diffusivity of dissolved iron (Lister, 1976).

A computer program was written to solve Equation (8) iteratively. The solution involves evaluating the film thicknesses at each time step from the balance equations for iron in each layer:

$$0.723\frac{d\delta_i}{dt} = 0.476(1-\Phi_i)\frac{dm}{dt} \quad (9)$$

$$0.723\frac{d\delta_o}{dt} = k_p F^*(C_b - C^e_{O-C}) \quad (10)$$

At each time step, the potentials at the M-O and O-C interface are evaluated from the electrochemical parameters of the process (as described later) and are used to adjust C^e_{M-O}, C^e_{O-C} and k_p, since these quantities depend on potential. The electrochemical treatment includes the effects of generated hydrogen.

Erosion of the oxide is considered in the computation by means of an empirical spalling term. A reciprocal distribution of size of oxide crystallites is assigned to each layer (other distributions such as normal or lognormal gave unsatisfactory results). For the inner layer, the sizes range from 10 nm (Mayer, 2001) to one half the layer thickness in intervals of 10 nm, while for the outer layer the range is from 0.1 □m to the complete layer thickness in intervals of 10 nm. A random number generator is used to select a size of particle to spall, and the time taken for that particle to spall is assumed to be directly proportional to the particle size and inversely proportional to the fluid shear stress at the wall. The latter is determined at the appropriate coolant and geometrical conditions by the well known Moody correlation, which at the high Reynolds numbers pertinent to feeder flows indicates that shear stress is proportional to the square of the velocity. The constant of proportionality in the erosion term is determined by fitting the model to the data of Kenchington et al. (1983) which, as mentioned before, were obtained from loop experiments under conditions of iron-saturated coolant flowing at high velocity.

The computer program iteratively evaluates the corrosion and oxide film build up at each time step until the time for a spalling event is reached, when the oxide thickness instantaneously drops by the requisite amount and the oxide build up recommences. For the double-layer oxide of the inlet feeders, the inner layer is not allowed to spall unless the outer oxide has coincidentally spalled to zero thickness – an extremely rare occurrence in the modelling. Note that the description strictly speaking applies to one spot on the feeder surface; however, the behaviour is applicable to the whole surface (with the appropriate boundary conditions) since the stochastic nature of the spalling process averages out differences between events at adjacent spots.

Transport Equations for FAC (Outlet Feeders)

The treatment is the same as that of the inlet feeders, except that there is no outer oxide layer and the inner layer dissolves at the O-C interface. Note that the computations show that the driving force for dissolution persists throughout the outlet feeders and headers (despite the input of dissolved iron along the corroding pipework) and well into the steam generators, where there is negligible iron input but the saturation concentration falls because of the temperature reduction.

The corrosion rate is given by:

$$\frac{dm}{dt} = \frac{S.C^e_{m-o} - \dfrac{(k_d F^* C^e_{O-C} + kC_b)}{(k_d F^* + k)}}{0.476(1.101+\Phi_i)\left[\dfrac{\delta_i \zeta}{\rho_{ox}(1-\Phi_i)\Phi_i D_{Fe}} + \dfrac{1}{(k_d F^* + k)}\right]} \quad (11)$$

where: k_d = dissolution rate constant (initially assumed same as Balakrishnan's (1970) value) and the other symbols have their meaning as before but their value is appropriate to the outlet feeder conditions.

Again, the computer program solves for corrosion rate and film thickness iteratively at each time step, using the iron balance equation for the dissolving (inner) layer:

$$0.723\frac{d\delta_i}{dt} = 0.476\frac{dm}{dt}(1-\Phi_i) - k_d F^*(C^e_{O-C} - C_b) \quad (12)$$

and again, the electrochemical quantities C^e_{M-O}, C^e_{O-C} and k_d are adjusted for the computed potential at each step.

The spalling criteria in the erosion term must now include the effects of oxide dissolution which weaken the film and make erosion easier. The particle size distribution is assumed to be the same as that for the inner layer of the inlet feeders, viz., agglomerates of 10 nm crystallites distributed reciprocally. The time between spalling events is assumed to be proportional to the size of particle spalled and inversely proportional to the fluid shear stress at the wall (as with the inlet feeders but with a surface roughness appropriate to 0.2 mm-deep scallops) and also to be inversely proportional to the dissolution rate. The dissolution factor makes the erosion dependent on potential. The erosion proportionality constant was deduced by fitting the model results to measurements of film thickness and corrosion rate made on feeder S08 removed from the Point Lepreau reactor (Lister et al., 1998).

Electrochemical Considerations

The six steps involved in the overall FAC process are illustrated in Figure 3. Our version of the pores-solution model, as just described, incorporates the effects of potential on four of the five steps that are electrochemical - corrosion, precipitation, dissolution, hydrogen production and erosion. An electrochemical relationship is not required for precipitation, since that is described by Equation 6. Diffusion involves the uncharged species $Fe(OH)_2$ in solution (Tremaine and Leblanc, 1980) and is not affected by potential. Note that the treatment of the general corrosion of inlet feeders is similar, except that there is no dissolution step (rather, an outer layer precipitation) and the erosion term, being devoid of a dissolution requirement, has no electrochemical component

For the electrochemical processes involved, the rate as an equivalent current, i, is described in terms of Butler-Volmer kinetics:

$$i = i_o\left\{\exp\left[\frac{\beta nF}{RT}(E_\ell - E_{eq})\right] - \exp\left[-\frac{(1-\beta)nF}{RT}(E_\ell - E_{eq})\right]\right\} \qquad (13)$$

where: i_o = exchange current;
β = symmetry coefficient (assumed 0.5);
n = number of electrons involved in process;
F = Faraday's constant;
R = gas constant;
T = absolute temperature;
E_ℓ = local potential;
E_{eq} = equilibrium potential.

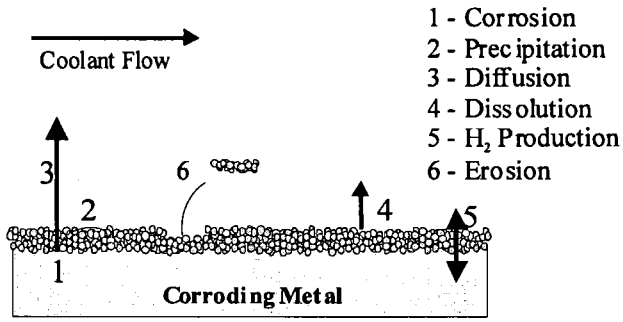

Figure 3. Six Steps of the FAC Mechanism

The current, i, is related to the rate of the process by Faraday's law. For example, the corrosion current, i_{corr}, is related to the corrosion rate by:

$$i_{corr} = \frac{nF}{M}\cdot\frac{dm}{dt} \qquad (14)$$

where M is the molecular weight. The appropriate local potential at the M-O interface is the corrosion potential, E_{corr}.

The Nernst equation written in terms of the system parameters and the appropriate species concentration provides the equilibrium potential E_{eq}. Again for the corrosion reaction at the M-O interface:

$$Fe + 2H_2O \; 6 \; Fe(OH)_2 + 2H^+ + 2e \tag{15}$$

So that:

$$E_{eq} = 0.14 - 1.98 \times 10^{-4}.T.pH + 4.13 \times 10^{-5}.T.\ln C^{e}_{M-O} \tag{16}$$

The standard potentials employed in the Nernst equation evaluations such as Equation 16 are obtained from the appropriate Gibbs energy of formation, □G (NBS Tables, 1982), as follows:

$$E^{\circ} = \frac{\Delta G}{nF} \tag{17}$$

The exchange current is given by (Bockris and Reddy, 1970):

$$i_o = \frac{Fk_BT}{h} \exp(-\frac{\Delta G^{\circ}_F}{RT}) \cdot C \cdot \exp(\frac{\beta nF}{RT} \cdot E_{eq}) \tag{18}$$

where: k_B = Boltzmann's constant;
h = Planck's constant;
ΔG°_F = free energy of activation;
C = species concentration.

At the M-O interface, ΔG°_F for Equation 18 is put equal to 144.6 kJ/mol after trial and error determination, and the starting value for C in the computation is the Tremaine and Leblanc (1980) solubility value for iron at the conditions of interest (the pH at the M-O interface is assumed equal to that of the bulk coolant). The M-O interface is therefore treated like an electrode in contact with a solution and the whole surface is assumed to be wetted, allowing anodic and cathodic processes to occur there according to Wagner-Traud principles. Note that, since the corrosion current from Equation 13 is defined by the corrosion rate in Equation 14, the assumption of Butler-Volmer kinetics determines the corrosion potential at the M-O interface, which is also the potential pertinent to the other processes at the interface. Thus, the oxide precipitation constant, k_p in Equation 8, is modified by the Vermilyea (1966) expression:

$$k_p' = k_p \exp(\frac{\beta nFE_{\ell}}{RT}) \tag{19}$$

and the solubility through the Nernst equilibrium expression.

At the O-C interface, the cathodic dissolution reaction equivalent to Equation 3 is written:

$$Fe_3O_4 + 2H_2O + 2H^+ + 2e \; 6 \; 3Fe(OH)_2 \tag{20}$$

The rate is determined by a Butler-Volmer relation – Equation 13 with parameters i_o, E_{ℓ} and E_{eq} appropriate to Equation 19 at that interface. The Nernst equation supplies E_{eq}:

$$E_{eq} = -0.75 - 1.98 \times 10^{-4}.T.pH - 1.29 \times 10^{-4}.T.\ln C_b \tag{21}$$

and Equation 18, with C_b and with a free energy of activation put equal to 120 kJ/mol after trial-and-error determination, supplies the exchange current.

The balancing anodic reaction at the O-C interface is hydrogen consumption:

$$H_2 \; 6 \; 2H^+ + 2e \tag{22}$$

To find the appropriate concentration of hydrogen at this interface, its production at the M-O interface and diffusion to the bulk coolant, where its concentration is assumed to be the same as the nominal concentration of

added gas (within the specification of 3-10 cm^3/kg), are taken into account. The rate of production due to corrosion at the M-O interface is obtained from the stoichiometry of the reaction equivalent to Equation 15 as (Johari, 1996):

$$H_2 \text{ generation} = 5.66x10^{-3} \frac{dm}{dt}(1-\Phi_i) \tag{23}$$

and the rate of consumption at the O-C interface is obtained similarly from the dissolution reaction (equivalent to Equation 20). Once the concentration at the O-C interface has been determined by a simple flux balance, which utilizes high-temperature diffusivities of hydrogen as obtained from the Eyring expression (Ferrell and Himmelblau, 1967) and assumes that 90% of produced hydrogen is dissipated through the metal, it is used in the Nernst equation to determine the equilibrium potential (note that the high mass transfer rates make the concentration at the O-C interface close to that in the bulk). The hydrogen concentration is also inserted into the exchange-current expression (Equation 18), which assumes a trial-and-error value of 90 kJ/mol for the free energy of activation. The Butler-Volmer equation can now be applied to describe the hydrogen reaction rate.

The potential at the O-C interface is determined by equating the anodic current (from hydrogen consumption) to the cathodic current (from oxide dissolution). The result is:

$$E_\ell = 2.58x10^{-4}.T.\ln\left[\frac{i_{ocath}\exp(\frac{1934}{T}E_{eqcath}) + i_{oan}\exp(\frac{1934}{T}E_{eqan})}{i_{ocath}\exp(\frac{-1934}{T}E_{eqcath}) + i_{oan}\exp(\frac{-1934}{T}E_{eqan})}\right] \tag{24}$$

The potential affects the oxide dissolution rate constant, as it does the precipitation constant at the M-O interface (Equation 19), though the Vermilyea (1966) expression and affects the solubility through the Nernst equation.

Mass Balance and Computation Around the Coolant Circuit

The primary circuit is divided into a number of nodes for the computation, as illustrated in Figure 4. Since corrosion rates are low in the inlet feeders and there is little effect of velocity, one length of piping between the steam generator outlet and the reactor inlet is considered representative. The large diameter piping between the steam generator outlet and the reactor inlet header has two nodes (one of the four primary heat transport pumps is located here) and the inlet feeder has four nodes.

The two loops of the primary circuit are nominally identical and the 190 fuel channels of each are symmetrically arranged in the reactor core; 95 fuel channels and their respective outlet feeders therefore represent the system. These feeders are divided lengthways into five nodes and are connected to the outlet header which leads to the steam generator inlet via large diameter piping. The steam generator bundle of U-tubes is divided into 18 nodes.

The node lengths in the feeders vary because the feeder geometry varies. The length is anywhere between 8.8 m and 19.0 m, some are constant in diameter but most of the outlet feeders have an expansion ("diffuser") towards the outlet header.

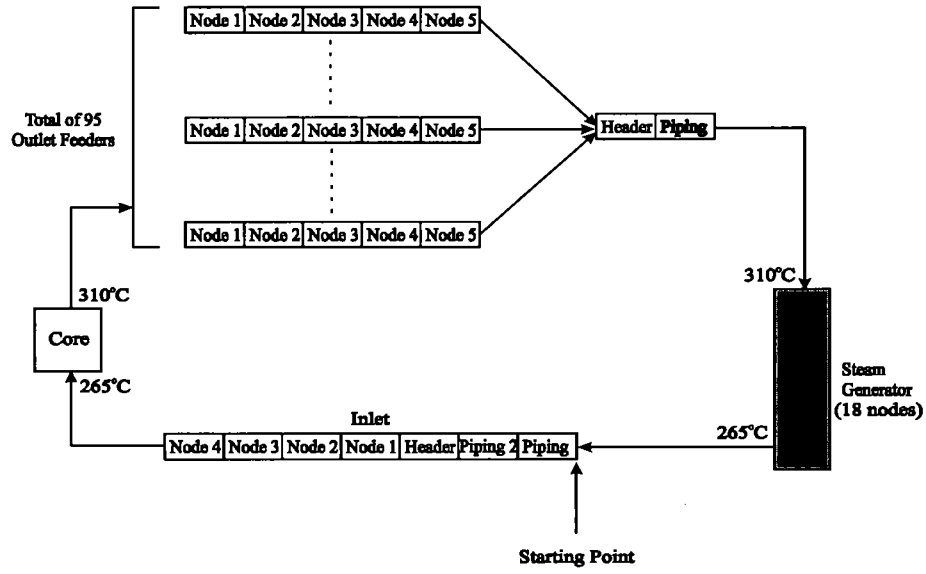

Figure 4. Node Diagram of CANDU Primary Circuit.

The first node of an outlet feeder constitutes the first 15 cm or so between the Grayloc connector and the first bend while the second node constitutes the next 15 cm or so around the bend. The bends are mostly through a 73°C angle but several are 42°C.

At each node, the corrosion equations are solved numerically and the nodes are linked around the circuit through the basic balance equation for dissolved iron:

$$\frac{\partial C_b}{\partial t} + V\frac{\partial C_b}{\partial x} + \frac{4}{d}(O - C) = 0 \qquad (25)$$

where V is the coolant velocity, d is the pipe diameter and $O - C$ is the oxide-coolant transport $(-k_p F^* (C_b - C^e_{O\text{-}C})$ for the inlet feeders from Equation 10 and $k_d F^* (C^e_{O-C} - C_b)$ for the outlet feeders from Equation 12). Note that in the core and the steam generators no corrosion processes are modelled. Since the coolant pH is maintained greater than that of minimum solubility of iron, the coolant becomes progressively undersaturated in iron as it is heated in its passage through the core; it then approaches and exceeds saturation as it is cooled in the steam generators, where it precipitates magnetite. A removal term, equivalent to a typical CANDU-6 clean-up half life of 1h, is incorporated in the circuit computation. This prevents eroded particles, which have no surface interactions in the current model, from increasing in concentration indefinitely.

While the erosion term for straight pipe is calculated from the fluid shear stress at the wall as determined by the Moody friction factor correlation (mentioned earlier), the outlet feeder bends are modelled with a computational fluid dynamics code ("FLUENT") to produce enhancement factors for the fluid shear stress at the rather severe geometries at the bend extrados (Callamand, 1999). Moreover, for one particular outlet feeder (designated F11, which at Point Lepreau has been thoroughly inspected for wall thickness along about 10 m of its length) FLUENT is used to estimate fluid shear stress in detail along the length and around the circumference. It should be noted, however, that the coolant flows in the individual feeders are not measured but obtained from computations with the thermalhydraulic code NUCIRC (Soulard, 1994). They are therefore somewhat uncertain.

The computation starts at Node 1 of an outlet feeder with the initial dissolved iron concentration at 310°C (C_b) put equal to the saturation value at the core inlet temperature of 265°C, as determined using the Tremaine and Leblanc (1980) data. For time steps of 1h, the equations are solved iteratively with a fourth-order Runge-Kutta routine, convergence usually being achieved within four iterations. The results for each time step therefore furnish values for metal loss, film thickness, interfacial potentials and the new C_b. The potentials are used to adjust the dissolution and precipitation constants and the solubilities for the following time step. If the random-number selection technique indicates that a particle spalling/erosion event occurs within the time step, the film thickness is adjusted accordingly.

The procedure is followed for successive time steps up to the total time specified, and then the computation recommences at Node 2, the pertinent input value for C_b being supplied by the results from Node

1. In this fashion, all 32 nodes from the core outlet to the core inlet are dealt with. As mentioned earlier, the Alloy-800 of the steam generator tubing is assumed not to corrode, but magnetite precipitation occurs when the cooling reduces iron solubility sufficiently – about half-way round the U-tube bundle. Precipitation occurs also in the inlet feeder, forming a Potter-Mann double layer of magnetite, and erosion there is a rare event. The equations for the inlet feeder are adjusted to accommodate precipitation accordingly.

It should be noted that all feeders are assumed to have a double-layer oxide film at the start of the corrosion. This corresponds to the film laid down during the preconditioning at reactor startup. The inner and outer layer are both 0.5 □m thick and the start of the corrosion process for the outlet feeders after the reactor startup entails the removal of the outer layer by dissolution and erosion before the inner layer is attacked. The diffusional resistance of both layers is accounted for in the transport equations until the outer layer has disappeared.

Results and Discussion

The steady-state corrosion potential, optimised as an intermediate step in the computations, for the extrados of the first bend of the outlet feeders ranges from -423 mV (vs. SHE) for the lowest corrosion rate (50.2 □m/a for feeder R03) to –342 mV for the highest corrosion rate (123.1 □m/a for feeder O06). The logarithm of the corrosion rate increases approximately linearly with potential – as expected for steel corroding actively. It will be recalled that the potential modifies the oxide solubility at the M-O interface; it increases it from the assumed initial value in the computation of 1.15×10^{-9} g/cm^3 (from the appropriate Tremaine and Leblanc (1980) data) to produce a concentration driving force sufficient to sustain the required diffusion of iron through the oxide film (a 10% enhancement is also included to account for the small crystallite size – the factor S in Equations 8 and 11). The solubility increase due to potential ranges from a factor of 5.4 at the highest corrosion rate to 10.9 at the lowest. At the O-C interface, the potential equivalent to the oxide dissolution and hydrogen consumption reactions is almost constant for all feeders at –342 mV. For a typical inlet feeder, the optimized corrosion potential averaged over 15 equivalent full power years (EFPY) is –333 mV and the potential at the O-C interface equivalent to oxide precipitation and hydrogen evolution is –229 mV.

These potentials are high, especially since the assumed cathodic process is hydrogen evolution. This mostly reflects uncertainty in the values of activation energy assumed for the electrochemical equations, to which the system is sensitive. Knowledge of other parameters in the model, such as oxide physical properties and dissolution/precipitation rate constants over the range of conditions considered, along with more precise values of coolant flows, would also help the accuracy of the model. It is interesting, however, that the recent cracking of a few outlet feeders at the Point Lepreau CANDU is raising speculation that the ECP close to the core is higher than previously assumed, possibly because of transient radiolytic species which would influence the cathodic reactions.

Nevertheless, as parameters in the computation, the potentials lead to realistic predictions that agree well with plant observations. Thus, Figure 5 presents the predicted oxide film build-up for three representative outlet feeders, T05, K02 and S08 with respective coolant velocities 10.4 m/s, 12.3 m/s and 16.2 m/s (it will be remembered that S08 was the removed feeder at Point Lepreau that was used to bench-mark the model; it had an average oxide thickness of about 0.8 □m (Burrill and Cheluget, 1998)). All these feeders are of 6.4 cm piping and all have a 73° first bend close to the Grayloc connector. The predictions are for the extrados of that bend.

Each diagram shows the initial build up towards "steady-state" thickness on a different time scale from the remainder of the exposure, which was taken to 15 EFPY. Because of its coarseness, the initial outer oxide layer from preconditioning is removed relatively quickly by dissolution and erosion. It is a poor barrier to diffusion so its major influence on the initial corrosion behaviour before it disappears is to protect the inner layer from erosion. The stochastic nature of the erosion process is indicated by the "spikiness" of the graphs. Note that, although individual spalling events can be seen in the initial period of each graph, the scale of the remaining period is so compressed as to show only instantaneous values of film thickness at the times plotted. Each diagram is calculated for one node in a feeder and can be viewed as the behaviour of the oxide at one point; an adjacent point will have the same overall pattern, but the details will be different. In other words, the spikiness reflects the surface micro-roughness – even though it is a temporal variation. It is interesting to note that the spalling of large particles that would remove substantial portions of the oxide is a rare event; the range of predicted micro roughnesses is between about 0.4 □m and 1.2 □m and the roughness decreases with decreasing film thickness, which in turn decreases with increasing flow rate.

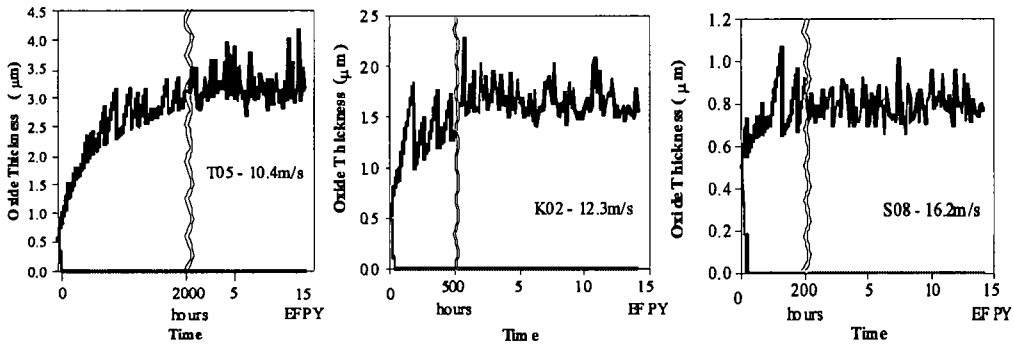

Figure 5. Predicted Oxide Film Buildup on Outlet Feeders.

The predicted steady-state corrosion rates and average film thicknesses for six representative feeders, including T05 and S08, are presented in Table 1. All six feeders are of 6.4 cm piping and all predictions are for the extrados of the first bend - which is 73° except for feeder R03, where it is 42°.

Feeder	Diameter (cm)	Bend Angle (°)	Coolant Velocity (m/s)	Film Thickness (□m)	Corrosion Rate (□m/a)
R03	6.4	42	10.5	5.0	50.2
T05	6.4	73	10.4	3.2	59.0
K02	6.4	73	12.3	1.7	75.6
F06	6.4	73	15.6	0.85	105.9
S08	6.4	73	16.2	0.80*	110.0*
O06	6.4	73	17.5	0.67	123.1
B08	5.0	42	15.8	1.1	94.9
B06	5.0	73	11.9	1.7	74.8

* measured values for feeder S08 removed from Point Lepreau – used to bench-mark model.

Table 1. Predicted Steady-State Corrosion Rate and Oxide Film Thickness at the Extrados of the First Bend of Outlet Feeders with Various Coolant Velocities.

The variation of predicted steady-state corrosion rate with average oxide film thickness is presented in Figure 6. Results for all outlet feeder geometries and coolant velocities fall on the same line. As expected, the thinner oxides formed at the higher flow rates present less of a barrier to diffusion, so corrosion rates are correspondingly higher. It is interesting to note that the relationship is not reciprocal, as might be expected from a completely diffusion–controlled mechanism with constant driving force. It appears that the electrochemical processes are sustaining higher corrosion rates than expected when the oxide is relatively thick.

The variation of predicted corrosion rate with coolant velocity is included in Figure 2, where it can be seen that the prediction is quite close to the early correlation from Point Lepreau. In fact, the main reason for the deviation is that the measurements of feeder S08, which bench-marked the model, do not themselves fall on the correlation line.

The effect on feeder corrosion rate at the bend extrados of reducing the bend angle is shown in Table 1, where feeders R03 and T05 have almost the same coolant velocity but bend angles of 42° and 73° respectively. The lower turbulence and fluid shear stress in R03 lead to a 15% lower corrosion rate than that predicted for T05. Table 1 also contains predictions for the 5.0 cm feeders B06 and B08 with a 73° and a 42° bend respectively. The trend is very similar to that of the 6.4 cm feeders.

For three of the 6.4 cm diameter feeders in Table 1, steady-state corrosion rates have been predicted all along the length. As shown in Figure 7, feeders T05, K02 and O06 have corrosion rates at the first bend corresponding to those in the table but the rates then drop with distance as the flow becomes fully developed and, with a lesser effect, as the iron concentration builds up in the coolant. The feeder in Figure 7 with the highest velocity coolant, O06, has the highest upstream corrosion rates but, because an expansion to 8.9 cm at about 5 m, it has the lowest downstream corrosion rates. It is easy to see from Figure 7 why measurements at the reactor of wall thickness at the header end of the feeders would not indicate FAC of the magnitude experienced at the first bend. However, the field instruments with accuracies between 25 □m and 75 □m should have picked up a total predicted wall thinning of about 400 □m over 12 years of monitoring. Why no corrosion at all was seen (Lister et al., 1994) is not understood.

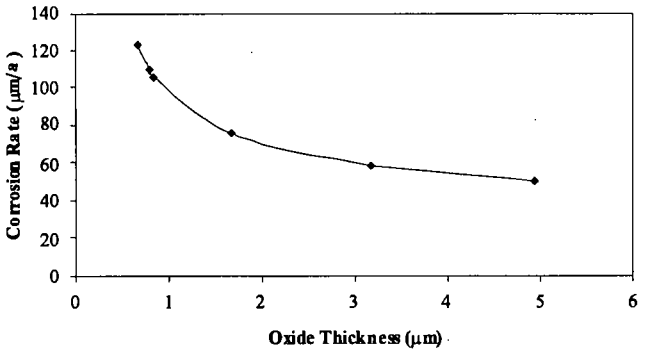

Figure 6. Predicted Variation of Steady-State FAC Rate with Oxide Film Thickness.

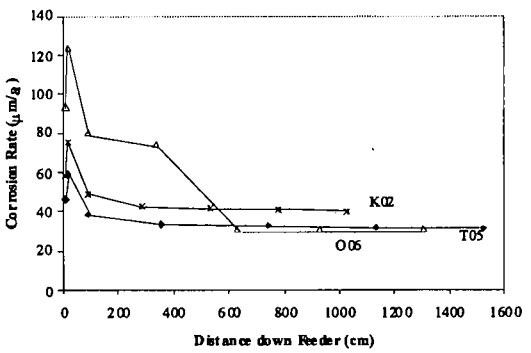

Figure 7. Predicted Variation of Steady-State FAC Rate with Distance Along the Feeder.

The 6.4 cm-diameter outlet feeder F11, which underwent extensive wall thickness measurement in the neighbourhood of the first two bends at the Point Lepreau Reactor, was modelled at four locations around the circumference to a distance of about 30 cm downstream of the Grayloc. As shown in Figure 8, predictions of local corrosion rate agree well with the measurements. It is of note that the maximum corrosion occurs at the bend intrados – particularly at the second bend, which experiences an accentuation of corrosion because of the streaming effect from the first bend. This is a direct consequence of the shear stress distribution for two-phase flow in the pipe, as modelled with the FLUENT code (Callamand, 1999).

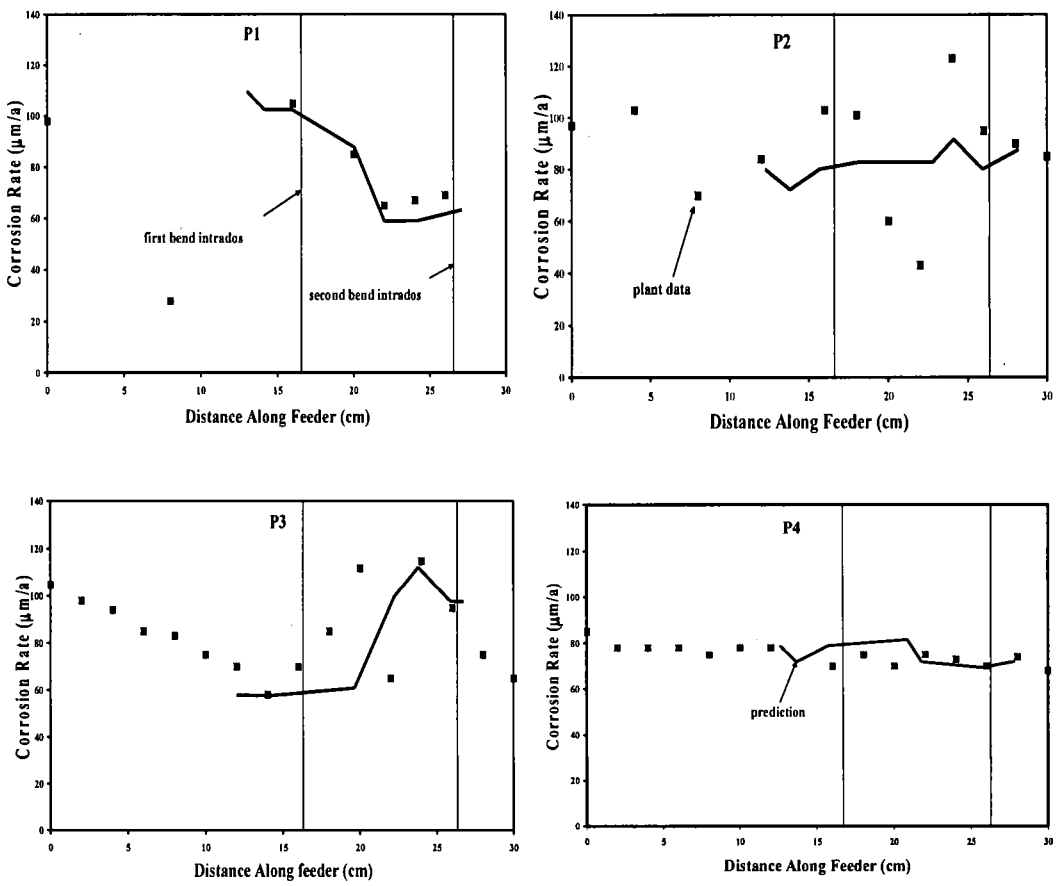

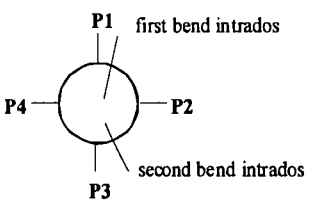

Figure 8. Predicted FAC Rate Around the First Two Bends of Feeder F11.

For the inlet feeders, there is no oxide dissolution, particle spalling events are rare and the effect of coolant velocity is minor. Corrosion and oxide film growth therefore vary little across the core and the behaviour of one feeder is taken as typical. Figure 9 presents the predictions for an inlet feeder over a 30 year exposure. The inner and outer oxide layers grow steadily from the preconditioning value of 0.5 □m to about 40 □m over the period, with very similar general patterns. Only the outer layer is affected by erosion – and then only rarely (six spalling events are captured in Figure 9) – leading to an oxide "roughness" of about 3 □m. The corrosion rate is predicted to drop rapidly during the first year but thereafter at a steadily decreasing rate; after 12 years the rate is 1.8 □m/a and after 30 years it is 1.5 □m/a. No corrosion measurements from inlet feeders are available for a detailed comparison with the predictions, but it is interesting to note that a section of inlet feeder removed from the Pickering CANDU reactor some years ago had oxide thicknesses up to 80 □m after ten years or so of operation. Unfortunately, the chemistry conditions to which the pipe was subjected before removal are in doubt (Burrill, 1995).

The erosion of particles from both inlet and outlet feeders contributes to suspended oxides, or "crud" in the coolant. The computations of the model keep track of erosion events and sizes of particle removed, leading to a predicted steady-state source term of 240 ppb/EFPY for particles greater than 0.45 □m (the usual criterion for crud in operating reactors). When this source term is used in conjunction with a purification half-life of one hour for a CANDU-6 primary coolant, a crud level of 0.05 ppb is predicted. This value is quite reasonable for an operating plant, considering the uncertainties in measurements with long sample lines and errors arising from cooling samples before filtration (Barton et al., 2000), though information about source terms other than feeders and about sinks other than purification would improve the prediction if it were available.

In summary, the good agreement between the predictions of the model, which was bench-marked with measurements of one reactor feeder, and plant observations of corrosion rate and its variation with coolant hydraulics supports the fundamental premise of the model – that FAC is caused by dissolution of the protective oxide film so that erosion occurs more easily. The ability of the model to predict realistic crud levels adds weight to the argument for particle erosion. Furthermore, the successful treatment of both inlet and outlet feeders with their different environments and corrosion characteristics supports the detailed mechanisms underlying the model.

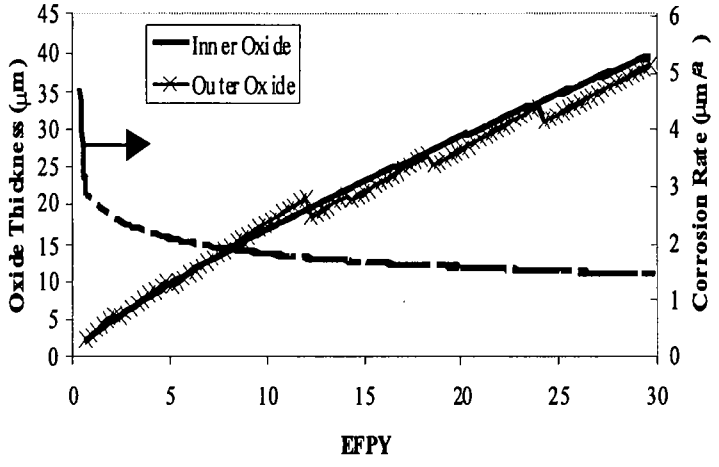

Figure 9. Predicted Oxide Thickness and General Corrosion Rate of an Inlet Feeder.

Conclusions and Summary

Flow-assisted corrosion (FAC) of carbon steel in high-temperature lithiated water can be described with a model that invokes dissolution of the protective oxide film and erosion of oxide particles that are loosened as a result. General corrosion under coolant conditions where oxide is not dissolved is described as well.

In the model, the electrochemistry of magnetite dissolution and precipitation and the effect of particle size on solubility move the dependence on film thickness of the diffusion processes (and therefore the corrosion rate) away from reciprocal. Particle erosion under dissolving conditions is treated stochastically and depends

upon the fluid shear stress at the surface. The corrosion rate dependence on coolant flow under FAC conditions then becomes somewhat less than that arising purely from fluid shear (proportional to the velocity squared). Under non-dissolving conditions, particle erosion occurs infrequently and general corrosion is almost unaffected by flow

For application to a CANDU primary circuit and its feeders, the model was bench-marked against the outlet feeder S08 removed from the Point Lepreau reactor, which furnished one value of film thickness and one of corrosion rate for a computed average coolant velocity. Several constants and parameters in the model had to be assumed or were optimised, since values for them were not available. These uncertainties are no doubt responsible for the rather high values of potential that evolved as steps in the computation.

The model predicts film thickness development and corrosion rate for the whole range of coolant velocities in outlet feeders very well. In particular, the detailed modelling of FAC in the complex geometry of one outlet feeder (F11) is in good agreement with measurements. When the particle erosion computations are inserted in the balance equations for the circuit, realistic values of crud level are obtained. The model also predicts low corrosion rates and thick oxide films for inlet feeders, again in general agreement with observations.

Acknowledgement

J. Slade and the NB Power staff at Point Lepreau are thanked for supplying data and for useful discussions. W. Cook and N. Arbeau at UNB are thanked for their criticisms and suggestions, while NB Power, Atomic Energy of Canada Ltd. and the Natural Sciences and Engineering Research Council are thanked for financial support.

References

Balakrishnan, P.V. A Radiochemical Technique for the Study of Dissolution of Corrosion Products in High-Temperature Water. Canadian J. Chem. Eng., 55, 357 (1977).

Barton, M., Conqueror, M.R., Garbett, K., Mantell, M.A., Phillips, M.E., Polley, M.V. and Westall, W.A. Corrosion Product Measurements at the Sizewell B PWR. Proc. 8th BNES Intern. Conf. on Water Chem. of Nuclear Reactor Systems. Bournemouth, U.K. (2000).

Berge, P., Ribon, C. and Saint-Paul, P. Effect of Hydrogen on the Corrosion of Steels in High Temperature Water. Corrosion, 32 (6), 223 (1976).

Berge, P., Ducreux, J. and Saint-Paul, P. Effects of Chemistry on Erosion-Corrosion of Steels in Water and Wet Steam. Proc. 2nd BNES Intern. Conf. on Water Chem. of Nuclear Reactor Systems. Bournemouth, U.K. (1980).

Berger, F.P. and Hau, K-F. F-L. Mass Transfer in Turbulent Pipe Flow Measured by the Electrochemical Method. Intern. J. Heat and Mass Trans., 20, 1185 (1977).

Bignold, G.J., Allen, P. and Hampson, N.A. The Effect of Electrical Potential on the Dissolution of Iron Oxide Crystals.(I) A Review of Selected Relevant Literature. Surface Techn., 7, 273 (1978).

Bloom, M.C. A Survey of Steel Corrosion Mechanisms Pertinent to Steam Power Generation. Proc. 21st Annual Water Conf., Eng. Soc. W. Pennsylvania, Pittsburgh, Pa., U.S. (1960).

Bockris, J. O'M. and Reddy, A.K.N. Modern Electrochemistry – An Introduction to an Interdisciplinary Area. Vol. 2. Plenum Press, New York, U.S.A. (1970).

Burrill, K.A. Private Communication. Atomic Energy of Canada, Ltd. (1995).

Burrill, K.A. and Cheluget, E.L. Corrosion of CANDU Outlet Feeder Pipes. Proc. JAIF Intern. Conf. on Water Chem. in Nuclear Power Plants. Kashiwazaki, Japan (1998).

Burrill, K.A. and Turner, C.W. Control of Reactor Inlet Header Temperature (RIHT) rise in CANDU. Proc. 2nd CNS/COG Intern. Steam Generator and Heat Exchanger Conf., Toronto, Canada (1994 June).

Callamand, S. FAC Studies. Progress Report to UNB and CNER (1999 July).

Castle, J.E. and Mann, G.M.W. The Mechanism of Formation of a Porous Oxide Film on Steel. Corros. Sci., 6, 253 (1966).

Castle, J.E. and Masterson, H.G. The Role of Diffusion in the Oxidation of Mild Steel in High Temperature Aqueous Solutions. Corros. Sci., 6, 93 (1966).

Effertz, P.H. Morphology and Composition of Magnetite Layers in Boiler Tubes Following Long Exposures. Proc. 5th Intern. Congress on Metallic Corrosion, Tokyo (1972).

Elliott, A.J. Private communication. Atomic Energy of Canada Ltd. (2000).

Ferrell, R.T. and Himmelblau, D.M. Diffusion Coefficients of Hydrogen and Helium in Water. A.I.Ch.E. Journal, 13 (4), 702 (1967).

Johari, J.M.C. Modelling Corrosion for Corrosion-Product Transport in CANDU Reactors and PWRs. M.Sc.E. Thesis, Dept. of Chem. Eng., University of New Brunswick (1996).

Kenchington, J.M., Pearson, B.M. and Murphy, E.V. Final Analysis of the Single Phase Erosion/Corrosion Test Programme for Reactor Inlet Feeders. Proc. Annual CNA Conference, Montreal, Canada. Canadian Nuclear Association, Toronto, (1983).

Lister, D. H. Mass Transfer in the Contamination of Isothermal Steel Surfaces, Nucl. Sci. and Eng., 61, 107 (1976).

Lister, D.H., Arbeau, N. and Johari, J.M.C. Erosion and Cavitation in the CANDU Primary Heat Transport System. Atomic Energy Control Board Report RSP-009 (1994).

Lister, D.H., Gauthier, P., Goszczynski, J. and Slade, J. The Accelerated Corrosion of CANDU Primary Piping. Proc. JAIF Intern. Conf. On Water Chem. in Nuclear Power Plants, Kashiwazaki, Japan (1998).

Lister, D.H., Slade, J. and Arbeau, N. The Accelerated Corrosion of CANDU Outlet Feeders – Observations, Possible Mechanisms and Potential Remedies. Proc. Annual CNS Conference, Toronto, Canada. Canadian Nuclear Society, Toronto (1997).

Mayer, P. Private Communication. Kinectrics, Kipling Avenue, Toronto, Canada (2001 May).

Potter, E.C. and Mann, G.M.W. Mechanism of Magnetite Growth on Low-Carbon Steel in Steam and Aqueous Solutions up to 550°C. Proc. 2nd Intern. Congress on Metallic Corrosion. National Assoc. Corros. Engnrs., Houston, (1963).

Poulson, B. Mass Transfer from Rough Surfaces. Corros. Sci., 30 (6/7), 743 (1990).

Robertson, J. The Mechanism of High Temperature Aqueous Corrosion of Steel. Corros. Sci., 29 (11/12), 1275 (1989).

Soulard, M. Private Communication. Atomic Energy of Canada, Ltd. (1994).

Sweeton, F.H. and Baes, C.F., Jr. The Solubility of Magnetite and Hydrolysis of Ferrous Ion in Aqueous Solutions at Elevated Temperatures. J. Chem. Thermod., 2, 479 (1970).

Tomlinson, L. Mechanism of Corrosion of Carbon and Low Alloy Ferritic Steels by High Temperature Water. Corrosion, 39 (10), 591 (1981).

Tremaine, P.R. and LeBlanc, J.C. The Solubility of Magnetite and the Hydrolysis and Oxidation of Fe^{2+} in Water at 300°C. J. Solution Chem., 9 (6), 415 (1980).

Vermilyea, D.A. The Dissolution of Ionic Compounds in Aqueous Media. J. Corros. Soc., 113 (10), 1067 (1966).